RESEARCH ARTICLE

ADVANCED HEALTHCARE MATERIALS
www.advhealthmat.de

Graded Hydroxyapatite Triply Periodic Minimal Surface Structures for Bone Tissue Engineering Applications

*Tejas M. Koushik, Catherine M. Miller, and Elsa Antunes**

Porous scaffolds in bone tissue engineering (BTE) play a crucial role in facilitating osteointegration with host tissues and providing nutrients to cells involved in bone healing. Scaffold architecture influences osteointegration, biofunctionality and mechanical strength, necessitating a clear understanding of its impact. In this study, hydroxyapatite scaffolds are 3D printed with three types of triply periodic minimal surface (TPMS) structures: gyroid, lidinoid, and split-P, at porosities ranging from 50% to 80%. Split-P architecture exhibits the highest compression strength, between 15 and 25 MPa, but provides the least surface area for bone apatite precipitation. Conversely, gyroid and lidinoid structures demonstrate the highest levels of bone apatite precipitation across all porosities when immersed in simulated body fluid. To optimise scaffold design, graded structures were designed with multiple TPMS structures arranged in a core-shell configuration. A structure featuring a solid core and a 70% gyroid shell achieves the highest compression strength of 120 MPa, while also supporting cell attachment and differentiation comparable to that of a fully porous structure. This combination of compression strength similar to cancellous bone and ability for positive interaction with osteoblast cells makes it an ideal candidate for load-bearing applications in BTE.

1. Introduction

Bone tissue engineering (BTE) involves the design and manufacturing of interconnected porous scaffolds to provide a suitable microenvironment for the growth of bone tissues and mechanical support. Permeability of the BTE scaffolds allows vascularization of bone tissues, to achieve high levels of permeability previous studies have recommended porosities >60%.[1,2] This requires increasing pore sizes, redistribution of pore size variations, and modifying scaffold geometry. However, these modifications reduce compression strength and, consequently, the load bearing ability of the scaffold. This rigid dichotomy of BTE scaffold requirements makes it extremely challenging to develop scaffolds that encourages osseointegration while still having the necessary mechanical strength suitable for the application.[2,3] Zhang et al.[4] showed that a hierarchically structured poly caprolactone surrounded with a hydrogel matrix (containing deferoxamine nanoparticles and MnCO nanosheets) can produce a positive effect in bone healing and produce compression strengths of 50–56 MPa. Jia et al.[5] showed that magnesium-based scaffolds with better interconnectivity and high porosities (>70%) showed very low compression strength (<3 MPa) but showed greater cell migration through the scaffold. These observations further confirm the challenge of satisfying the rigid dichotomy of BTE scaffolds.[6,7] Hydroxyapatite (HAp) is a commonly used bone replacement material. Due to its biocompatibility and chemical similarity to the mineral phase of natural bone tissue. Although these materials are resorbable, resorption is an extremely slow process.[8] Other calcium-based compounds such as tricalcium phosphates (TCP) and biphasic calcium phosphate (BCP) have been shown to undergo faster resorption. While the faster resorption can be beneficial, it could also result in a local pH change. Previous studies have shown that prolonged acidification can cause a reduction fibroblast proliferation and hence prevent would closures.[9] Alkaline environments on the other hand can exert positive cellular benefits suited for bone healing. Alkalinization can release of Ca^{2+} ions which influence intracellular events; release of growth factors and stimulation of glycolysis or a rise in ATP generation.[10,11] Collagen production is usually an energy intensive process, hence higher ATP generation can contribute to its effect on bone formation.[12] Resorption of these calcium-based compounds (HAp, TCP and BCP) has been shown to occur through two pathways; osteoclastic resorption during bone remodeling and chemical or physical delamination.[13] This process will only occur when the full surface of the scaffold is vascularized and

T. M. Koushik, E. Antunes
College of Science and Engineering
James Cook University
Townsville, QLD 4811, Australia
E-mail: elsa.antunes1@jcu.edu.au

C. M. Miller
College of Medicine and Dentistry
James Cook University
Cairns, QLD 4878, Australia

The ORCID identification number(s) for the author(s) of this article can be found under https://doi.org/10.1002/adhm.202402953

DOI: 10.1002/adhm.202402953

in contact with the surrounding medium. Surface area available for the resorption to occur on the BTE scaffolds will depend on their permeability and porosity. Resorption of calcium-based compounds (HAp, TCP, and BCP) over time will lead to a reduction in mechanical strength and making them unable to provide long-term mechanical support to a recovering patient.

High strength BTE scaffolds are commonly made from Ti6Al4 V, yttria partially stabilized zirconia, or other materials having mechanical strength >100 MPa are bioinert in nature. This lack of interaction makes them unsuitable to increase the efficacy of synthetic BTE scaffolds. Ceramic composites in the past decade (bioceramics) are increasingly being used as synthetic bone replacements. Knabe et.al[14] showed that silica containing calcium alkali orthophosphate used in critical sized defects in in vivo rat models produced higher bone fractions and osteoblast vascularization. Pierantozzi et al.[15] showed that HAp or strontium-substituted HAp (Sr-HAp) used along with poly caprolactone (PCL) stimulated higher levels of alkaline phosphatase (ALP) activity when compared to the PCL polymer. While the ALP activity generally declines with the formation of calcium deposits, the Sr-HAp PCL scaffold was able to retain ALP activity until the 14-day mark indicating a delay in osteogenesis. Mancuso et al.[16] showed that up to 10 wt,% inclusion of barium titanate ($BaTiO_3$) in PCL composite scaffolds showed an increase in mechanical strength while supporting cell growth and viability when cultured with human osteoblast cells. Further the inclusion of ceramic particles (HAp and $BaTiO_3$) in the scaffold showed the retention of the osteoblastic phenotype and deposition of bone-like extracellular matrix onto the scaffold surface. This bone apatite formation in vitro has been a crucial consideration in the choice of biomaterials for BTE applications as they provide an indication of the bone healing ability of scaffolds within a short time frame.[17,18] Simulated body fluid (SBF) tests have commonly been used for the measurement of bone apatite formation, and, while the conditions differ significantly from in vivo experiments, they can be used to predict performance of HAp ceramics.[17,19] Ca-P phases in aqueous solutions that have precipitated during the SBF test have been known to include dicalcium phosphate [$CaHPO_4.2H_2O$] (DCPD), octacalcium phosphate [$Ca_8(HPO_4)_2(PO_4)_4.5H_2O$] (OCP) and hydroxyapatite [$Ca_{10}(OH)_2(PO_4)_6$] (HAp). OCP and the DCPD are the precursors of HAp during the SBF test, but HAp is thermodynamically favorable to exist in the SBF solution.[20] During the course of immersion, there are multiple association and dissociation reactions that help drive the precipitation of Ca-P phases on the scaffold surface; previous studies[20–23] have only considered the chemical properties of the SBF fluid and substrate. However, the nucleation rate of the Ca-P on the surface of a scaffold will also depend on the extent of SBF intrusion. In this study, we intend to assess the effect of scaffold geometry and porosity on the Ca-P phase precipitation.

Periodic lattice structures have been popularly used in tissue engineering applications due to their ability to be engineered based on the required porosity, structure and load bearing capacity.[24] Examples of these lattices used specifically for bone tissue engineering application include voronoi, cubes, octets, and honeycomb lattices.[25] Triply periodic minimal surfaces (TPMS) have recently become a popular choice for use in BTE applications due to their ability to mimic the internal geometry of natural bone tissues along with an optimal combination of strength and porosity.[2] Gyroids have been a popular choice for use in BTE applications due to the unique combination of permeability and strength offered by the structure.[2] Germain et al.[26] showed that gyroid-based scaffolds exhibited an isotropic stress response under compression and also showed high structural retention (up to 64 weeks) during aging in suitable physiological conditions. This was attributed to the greater contact area between layers and interconnectivity compared to strut-based lattice structures. Zhang et al.[27] showed that non gyroid-based structures such as split-P, diamond, and schwarz structures offered high compressive strength across all pore sizes when compared to gyroids. The split-P structure showed the highest energy absorption across all pore sizes (300–900 μm) and concave surfaces of the split-P structure promoted osteogenic cell differentiation compared to the flat surfaces of a cross-hatch lattice. Lidinoid structures tended to show higher porosity compared to other TPMS structures for the same pore sizes (300–900 μm).[27] Feng et al.[28] showed that combining IWP and P surface, a 30–55% improvement in stiffness could be achieved. Mechanical strength and permeability which are critical features of BTE scaffolds depend on scaffold architecture and porosity. While each of these TPMS structures have their unique advantages and disadvantages, a hierarchical arrangement of these multiple structures with varying porosities can be used to optimize the scaffold design for any requirement.[7] However, there are limited studies exploring the effect of porosity and geometry on the mechanical strength and bone apatite formation in TPMS structures.

In this study, stereolithography-based ceramic 3D printing was used to explore the effect of scaffold porosity and geometry of TPMS structures on their performance as BTE scaffolds. Mechanical strength of these different scaffold geometries (split-P, gyroid, and lidinoid) at different porosities (50–80%) was explored. In vitro testing was performed to assess bone apatite precipitation of the TPMS scaffold as function of scaffold structure and porosity. This study demonstrates the functionality of different TPMS structure for bone tissue engineering applications, providing a framework for creating hierarchical or composite structures for BTE scaffolds. Lastly, we have explored two different strategies for graded composite TPMS structures and examined their effect on cell proliferation and compression strength.

2. Experimental Section

2.1. TPMS Structures

Surfaces of the gyroid (GY), split-P (SP), and lidinoid (LI) TPMS structures used in this study can be defined using the equations in **Table 1**. From the previous work[24] it was identified that gyroid-based structures are known to provide high material efficiency providing superior mechanical strength at high porosities, similar to natural bone tissue. Lidinoid-based TPMS structures were chosen as they provide the maximum surface areas for cellular interaction. Lastly, split-P structures were chosen for their high compression strengths and stiffness.[27]

TPMS structures derived from the equations in Table 1 were mapped onto a cylindrical volume using nTopology. A cylindrical

Table 1. Surface functions of different (gyroid, split-P, and lidinoid) TPMS structures. Equations for the TPMS lattice were obtained from nTopology official website.

TPMS structure	Equation	References
Gyroid	$\sin(x)\cos(y) + \sin(y)\cos(z) + \sin(z)\cos(x) - t$	[29]
Split – P	$1.1*(\sin(2*x)*\sin(z)*\cos(y)+\sin(2*y)*\sin(x)*\cos(z)+\sin(2*z)*\sin(y)*\cos(x))-0.2*(\cos(2*x)*\cos(2*y)+\cos(2*y)*\cos(2*z)+\cos(2*z)*\cos(2*x))-0.4*(\cos(2*x)+\cos(2*y)+\cos(2*z))-t$	
Lidinoid	$\sin(2*x)*\cos(y)*\sin(z)+\sin(2*y)*\cos(z)*\sin(x)+\sin(2*z)*\cos(x)*\sin(y)-\cos(2*x)*\cos(2*y)-\cos(2*y)*\cos(2*z)-\cos(2*z)*\cos(2*x)+.3$	

volume was chosen to reduce stress concentration due to shrinkage during the sintering process. To produce different volume porosities (50–80%) within the cylindrical volume the wall thickness and mid-surface offset (shown in **Figure 1**) of each TPMS lattice type was modified using the values in **Table 2**. Wall thicknesses of lidinoid and split-P TPMS structures at porosities of 80% were <0.20 mm (recommended minimum thickness) and thus were excluded from the experimental analysis. Thickness <0.4 mm are easily damaged when excess slurry is cleaned from the green parts obtained after 3D printing.

2.2. 3D Printing of Scaffolds

All parts were 3D printed through stereolithography of ceramic slurries on the C100 EasyFab (3DCeram, France).[30] The parts were manufactured using photocurable HAp ceramic slurry supplied by 3DCeram. Processing parameters provided by the manufacturer were used for 3D printing the parts using the HAp feedstock. Excess slurry was cleaned using an air brush prior to debinding at conditions recommended by the manufacturer. Further the debinded samples were sintered at 1280 °C with dwell of 60 min and a heating rate of 3 °C min^{-1}. The sintered samples were cooled to room temperature at 3 °C min^{-1}. In addition to the TPMS scaffolds described in Table 2, solid cylinders (diameter = 10 mm and height = 3 mm) were fabricated for further characterization of the sintered HAp.

2.3. Characterization of Sintered Parts

Scanning electron microscopy (SEM, Hitachi SU5000) was used to characterize surface morphology and grain sizes. Discs for SEM were prepared using a series of grinding papers (180, 320, 600, 800, 1200, and 2500 grit) followed by polishing using a 1 µm diamond suspension and OP-S solution for up to 10 min each. The polished samples were thermally etched at 1180 °C for 60 min. Crystalline phases of the sintered HAp pellet were characterized using X-ray diffraction (XRD, Bruker D2 Phaser). The XRD scan was set between 10° and 80° with a step size of 0.02° and dwell of 1 sec/step. The density of the sintered samples was measured according to the procedure described in ISO 18 754 and compared with the theoretical density of HAp.

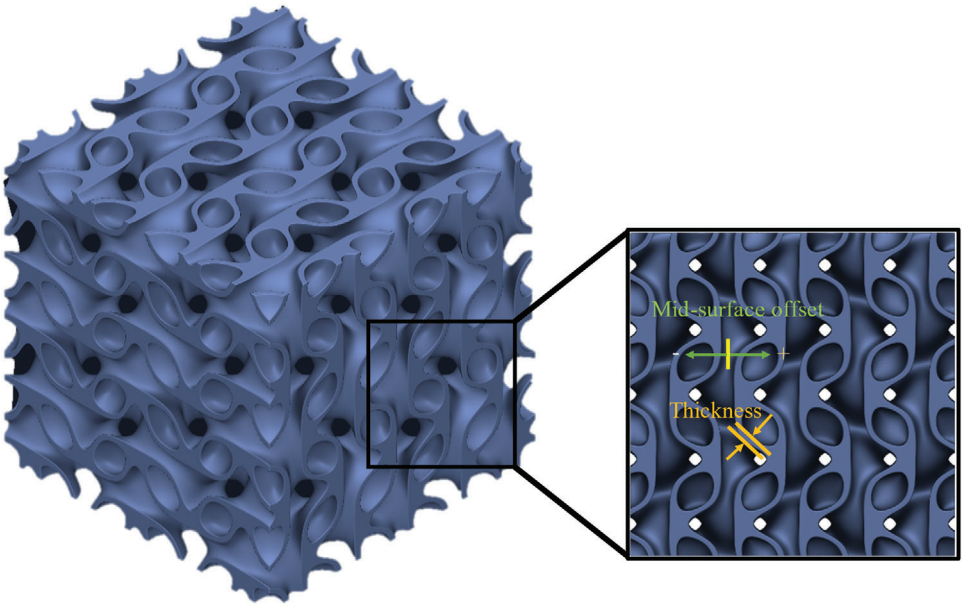

Figure 1. An example of a TPMS mapped onto a rectangular volume on nToplogy. Input variables such as mid-surface offset and thickness shown in the figure were modified to achieve the required volume porosity. Thickening the TPMS surface involves moving the surface by fixed distance. Mid-surface offset involves the movement of the mid-surface of the wall (shown in yellow) inward (+ve) or outward (−ve).

Table 2. TPMS lattice parameters used to obtain different porosity values in the mapped cylinder volume. Pore size of the produced lattices vary between 0.9 and 1.2 mm.

Unit cell type[a]	Porosity [Vol%]	Mid-surface offset [mm]	Wall thickness [mm]
GY	50	0.1	0.98
GY	60	0.2	0.78
GY	70	0.2	0.58
GY	80	0.25	0.38
LI	50	0.4	0.73
LI	60	0.41	0.6
LI	70	0.4	0.45
SP	50	0.19	0.79
SP	60	0.22	0.63
SP	70	0.2	0.62

[a] Note gyroid (GY), lidinoid (LI), and split-P (SP). Unit cell sizes were selected (4–5 mm) to achieve the required porosity at a suitable wall thickness.

2.4. Finite Element Modeling

ANSYS workbench 2023 was used to perform finite element analysis and determine the stress-strain response of the HAp scaffolds under uniaxial compression. The Youngs modulus and the Poisson's ratio of the HAp material was defined to be 10 GPa and 0.3, respectively.[27] A deformation of 0.01 mm (compressive) was applied to the cylinder keeping the bottom face fixed similar to a compression test. The stress, strain, and deformation along principal axis were recorded.

2.5. Compression Test

Compression test samples had a cylindrical shape with a height of 7 mm and a diameter of 7 mm. Ceramic parts were compressed at a crosshead speed of 0.1 mm min^{-1} to determine the compression strength and an average value was calculated from three tests.

2.6. Simulated Body Fluid

HAp parts of cylindrical shape with a height and diameter of 5 mm were fabricated as described in Section 2.2. The structures detailed in **Table 3** were soaked in a simulated body fluid (SBF) for a period of 5 weeks, change in concentration of Ca^{2+}, PO_4^{2-} along with Mg^{2+} was measured every week using ICP-MS. Oyane et al. showed that conventional SBF mimics the ion concentration and pH of human blood plasma, however, the solution deteriorates with time and hence is not suitable for long term in vitro assessment. Therefore, in this study ion concentrations of the SBF were modified as shown to prepare a stable solution suitable for in vitro assessment. Ion concentrations of the prepared solution compared to human blood plasma is shown in Table S1 (Supporting Information). The detailed process of preparation for this modified SBF has been described in Oyane et al.[31] To ensure that the ion concentration was similar to the values reported in literature, ICP-MS and pH electrode analysis was used to determine the ion concentrations of the prepared SBF solution.

Table 3. Volume of SBF fluid required for immersion of all TPMS scaffold structures.

Unit cell type	Porosity [Vol%]	Surface area [mm^2]	Volume of SBF fluid [mL]
GY	50	623.1	112
GY	60	621	112
GY	70	617.2	112
GY	80	611	112
LI	50	1065.4	160
LI	60	1079	160
LI	70	1104.4	160
SP	50	790	130
SP	60	796.4	130
SP	70	889.3	170

The minimum volume of SBF fluid required for soaking the samples is shown to be equal to half the surface area of the sample.[22] An additional 10 mL of SBF was added to account for the loss in volume during sampling done every week for 5 weeks. At the end of 5 weeks the TPMS scaffolds were weighed to determine the change in mass and the presence of the precipitates was investigated using SEM-EDS.

2.7. Proliferation Assay

Hydroxyapatite scaffolds of diameter 5 mm and height 3 mm were prepared using the 3D printing technique described in Section 2.2 for the proliferation assay. Based on the results from the compression testing and simulated body fluid tests, four structures were identified to create graded structures. The outer diameter of the scaffold is the section that is in direct contact with the surrounding tissue, therefore structures that showed maximum interaction with SBF were chosen (G70, L70, and G80). However, these structures showed the least compression strength compared to the other TPMS structures that were tested. S50 was chosen, therefore, to form the internal core with a diameter of up to 50% of the outer diameter (2.5 mm), as it showed the highest compression strength compared to all TPMS structures analyzed (shown in Section 3.2). To compare the performance of these graded structures, the chosen external geometries (G70, L70, and G80) were placed with a solid core of 50% diameter to the outer cylinder.

Seven structures shown in **Table 4** were 3D printed to determining cell attachment and proliferation of Human osteoblast cells (hOB; CRL-3602 ATCC, Manassas, VA, USA). Cells were expanded in culture flasks with complete media (CM) consisting of Dulbecco's modified Eagle medium (DMEM), supplemented with 10% fetal bovine serum (FBS) and 1% penicillin–streptomycin solution (Sigma–Aldrich, Castle Hill, NSW, Australia) incubated at 37 °C, 5% CO_2, and 90% humidity. Media was refreshed every 3 days, and the cells were passaged at 95% confluence as confirmed using conventional microscopy (Nikon Eclipse TS100, Nikon Instruments, Tokyo, Japan). For

Table 4. Hierarchical TPMS structures for cellular assay and compression testing.

Hierarchical structure	Internal geometry	External geometry	Surface Area [mm^2]
S50 – G70	S50	G70	686
S50 – L70	S50	L70	934.2
S50 – G80	S50	G80	680.4
Solid – G70	Solid	G70	523
Solid – L70	Solid	L70	818.7
Solid – G80	Solid	G80	525.7

experiments assessing cellular response, cells were lifted with trypsin (Sigma–Aldrich, Darmstadt, Germany) and seeded diluted to 1.7×10^6 cells per mL onto the structures. Cells were used between passages 5 and 6.

The hydroxyapatite scaffolds were placed in wells of a 48-well plate and 0.2 mL (containing 3.5×10^5 cells) of the cell suspension was added to each well to completely immerse the scaffolds. Further, 0.2 mL of the cell suspension was added in triplicate to wells without a scaffold to assess the effect of the scaffold material on cell attachment and proliferation. The well plates were then incubated at 37 °C at 5% CO_2 for 10 days.

Osteoblast cell proliferation is critically dependant on its environmental, mechanical, and chemical changes therefore providing an insight on the effects of scaffold geometry on the survival of the cells. Proliferation of the cells were assessed on days 1, 3, and 10 by measuring the reduction of resazurin to resofurin. Media from each of the specimens was transferred to a 96-well plate (in triplicate: 3 wells of 100 µl each), and the absorbance of resorufin (reduction product of resazurin) at 570 and 600 nm wavelengths was recorded using a microplate absorbance reader (iMark Microplate Absorbance Reader, Bio-Rad Laboratories, Hercules, CA, USA). The percentage of resorufin was calculated using the values obtained for stock solution (without cells). Measuring the reduction of resazurin to resofurin provides a direct and more sensitive measurement of cell viability compared to conventionally used MTT assay. Low toxicity and stability of the redox changes to the resazurin dye enables its use in long term cell viability studies.[32,33] Due to the permeability of the scaffold structures and low surface tension, seeded cells do not have sufficient time to undergo attachment. Hence to ensure that proliferation of the cells attached to the scaffold surface are measured, the structures were transferred into new wells 24 h after they were seeded with osteoblast cells.

Microscopy of the osteoblast cells present on the scaffold surface was carried to observe the extent of cell penetration and attachment on days 1, 3, and 10. The cell medium was drawn out and washed with PBS 2–3 times. The cells were then fixed using 3% paraformaldehyde (PFA) solution and set aside for 20 min at room temperature. The working solution for Abcam ifluor 594 was prepared using the manufacturer's protocol. The wells were then washed with PBS to remove any remaining PFA. Following which 100 µl of the previously prepared working solution along with 10 µl of DAPi were added and covered to prevent light exposure for 90 min. The cells were then imaged using an Olympus IX53 microscope with blue, green, and red fluorescence channels with a 10X objective.

2.8. Alkaline Phosphatase Assay

Alkaline phosphatase (ALP) activity of the osteoblast cells cultured on the structures described in Table 4 was measured using an ALP kit (ABCAM, Cambridge, United Kingdom). The structures were placed in a 24-well plate and seeded with osteoblast cells maintaining a cell density of 7×10^4 and incubated for 10 days. After day 10, cell lysates were collected according to the protocol specified by the manufacturer. Collected cell lysates were stored at −80 °C prior to measurement of ALP activity using a microplate absorbance reader (FLUOStar Omega, BMG Labtech (Offenburg, Germany)) at 405 nm.

3. Results and Discussion

3.1. Characterization of Sintered Parts

Average grain size of the sample was determined using the procedure highlighted in ASTM E112 -13 and was found to be 1.16 µm with a standard deviation of 0.03 µm. Density of the sintered samples was measured using the procedure highlighted in ISO 18 754 and samples were found to have a solid density of 94% ± 2% compared to the theoretical density of the HAp. The lack of full densification can be observed in the SEM image shown in **Figure** 2a, with an average pore size <2 µm. XRD results shown in **Figure** 2b showed peaks at 25.9°, 31.8°, 32.2° 39.6°, and 46.6° which are typically of HAp.

The stiffness matrix of each TPMS structure at different porosities (50–80%) was analyzed using nTopology and their distribution along the principle axis is shown in **Figure** 3. Elastic modulus of solid HAp has been reported to be in the range of 125–140 GPa, however, the 3D printed HAp sample was found to have an elastic modulus of 81.8 GPa.[34,35] Difference in elastic modulus arise from defects introduced during the sintering and microporosities (as shown in Figure 2a). At 50% porosity, differences between the highest and lowest stiffness values across all structures is <15% of the peak value, therefore stiffness distribution can be assumed to be close to uniform. This indicates lower chances of stress concentration during loading and hence higher compression strength across all TPMS structures at 50% porosity. The distribution of stiffness values becomes more anisotropic when increasing porosities from 50% to 80%, i.e., the difference between the lowest and the highest stiffness values increases up to 50% of peak value. Further, the maximum stiffness values lie along the principal directions leading to stress concentration and crack formation which can cause early failure in brittle materials such as HAp. Feng et al.[28] showed that material density distribution played a direct role in improving stiffness of a given TPMS surface. TPMS structures fabricated in Section 2.2, show a reducing lattice wall thickness as the porosity increases, leading to a reduction in material distribution density. Thus, making their responses more anisotropic when porosities increase from 50% to 80%. Khaleghi et al.[36] showed that this stiffness anisotropy could be minimized by appropriate selection of multiple TPMS structures in different ratios.

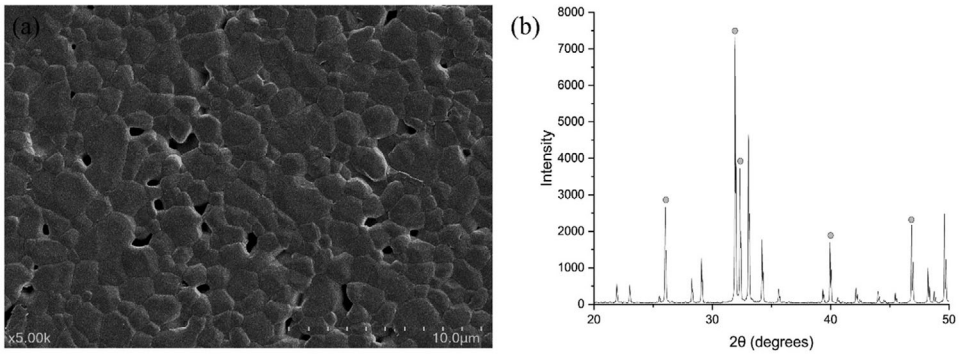

Figure 2. a) Microstructure of the sintered HAp parts shows the presence of pores <2 μm (b) Major XRD peaks observed at 25.9°, 31.8°, 32.2° 39.6°, and 46.6° are indicating typical HAp (based on ICDD 9–432).

Split-P structures tended to have the highest stiffness value [2–0.7 GPa] across all porosities indicating higher compression strengths, which is similar to results reported in previous studies.[27] Gyroid and lidinoid structures showed similar stiffness values at porosities 50–70%. At 80% porosity, stiffness offered by lidinoid is lower and anisotropic compared to the gyroid structure. Zhang et al.[27] showed that compression strengths of the gyroid and lidinoid structure were similar with increasing pore size from 300 to 900 μm.

Compression stresses are the primary forces experienced by BTE scaffolds, the above mentioned TPMS structures behave differently under compressive load. Finite element analysis of the different structures shown in Figure S6a (Supporting Information), gyroid structures undergo a combination of bend and stretch dominated failure at different regions of the same structure. As the deflections along x and y axis increase with applied compression forces, indicative of stretching along the X-Y plane. Some regions of the lattice undergo deflection along either x or y axis which is indicative of bending. In Figure S6b,d (Supporting Information) with lidinoid and split-p structures respectively, only undergo bend dominated failure. The bending or stretching of the lattice sections creates tensile forces leading to failure due to the brittle nature of HAp ceramics. Therefore, reduction of stiffness with increasing porosities leads to excessive bending or stretching of the lattices during compression causing it to undergo early failure.

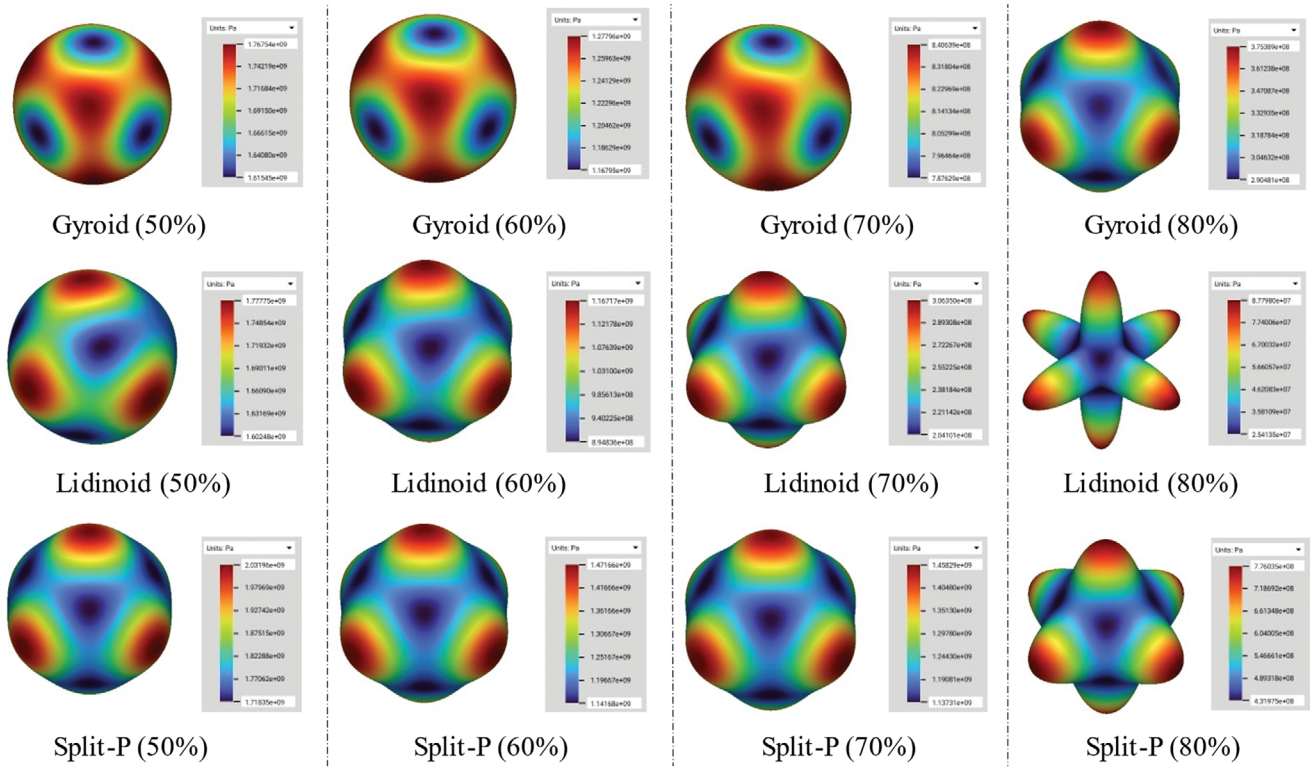

Figure 3. Effective Youngs modulus of gyroid, lidinoid, and split-P TPMS structures as a function of porosity.

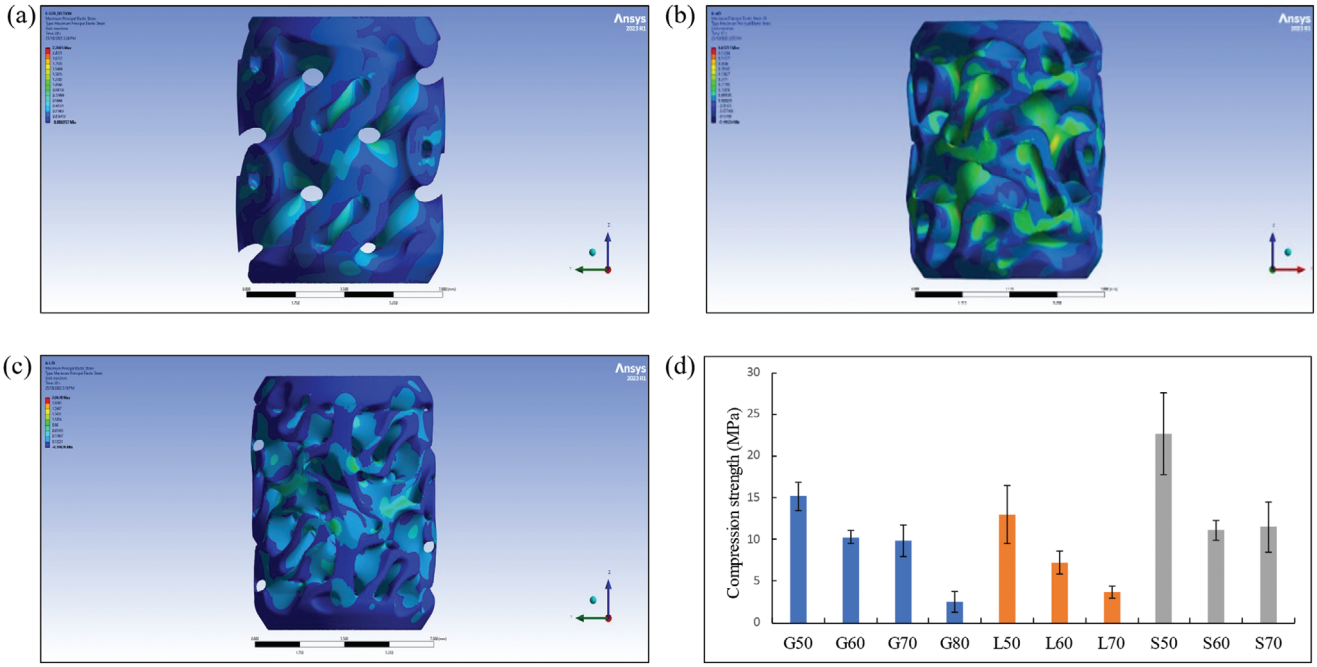

Figure 4. Maximum principal stress distribution observed in a) G60 b) L60 and c) S60. d) Compression strengths observed across all TPMS structures and porosities.

3.2. Compression Strength of TPMS Structures

Bone tissue can be classified into two types, the trabecular and cortical bones. The cortical bone segments are known to contribute more toward bone strength.[37] While the low strength of trabecular bone (2–12 MPa) helps in dissipating fracture energy during load transfer and the remaining spaces are filled with bone marrow/ECM.[38] Compression strength of the TPMS structures (gyroid, lidinoid and split-P) shown in **Figure** 4d is within a range of 2.5–25 MPa across all structures and porosities. This is within the range expected for trabecular bone but is insufficient to mimic cortical bone structures. Zhang et al.[27] showed that TPMS structures with porosities between 30% and 80% were able to achieve compression strength of 30–150 MPa through stereolithography of ceramic slurry. However, these compression strengths were achieved when the average pore size was less than or equal to 0.6 mm. In this study pore sizes of all structures were >1 mm reducing the achievable compression strength due to reduction in stiffness as discussed in Section 3.1. The presence of pores and defects in the ceramic matrix, is known to initiate crack formation and assist in crack propagation thereby reducing their compression strengths.[39] Therefore, these structures would require reinforcement prior to be used in load bearing areas.

To understand the effect of compression forces on TPMS structures it was simulated on the individual unit cells and their deformation response was observed in the principal directions. Gyroid structures predominately underwent stretch dominated failure with some amount of bending, causing the X and Y deflections to simultaneously increase with the applied load. Structures undergoing stretch dominated failures have high strength and stiffness but low energy absorption behaviour,[40] explaining why gyroid structures performed similarly to the split-P structures. Split-P and lidinoid structures shown in Figure S6 (Supporting Information) show a bend dominated failure, where the struts buckle when compressed. Under compressive loading, split-P structures exhibit demonstrably enhanced compressive strength due to the alignment of their constituent struts with the loading axis. Contrasting to this, lidinoid structures undergo premature failure in compression. This susceptibility can be attributed to the misalignment of their struts, which promotes catastrophic buckling events and the subsequent propagation of cracks through pre-existing porosity (shown in Figure S6b, Supporting Information), leading to structural collapse. Propagation of these cracks can be observed as large deflections on the stress-strain curves for the TPMS structures shown in Figure S5 (Supporting Information).

Gyroid structures (shown in Figure 4a) showed similar compression strength at porosities 50–70% due to the uniformly distributed stresses within the gyroid structures. Ceramics are generally brittle in nature therefore a plane stress condition can be assumed during compression, Figure 4a shows the accumulation of stresses at the struts in the gyroid structures. Therefore, localized bending of the unit cell at the bottom of the structures becomes first point of fracture, which is shown to propagate along the strut leading to final failure. Further the formation of X type double shear band can be observed during the compression of these structures. Compression strength of gyroid structures was observed to be between 13 and 15 MPa.

Lidinoid structures (shown in Figure 4b) showed a decreasing trend in compression strength with increasing porosities. Wall thickness of lidinoid structures were progressively reduced from 0.8 to 0.5 mm to achieve higher porosities (60% and 70%), and further the stiffness matrix shown in Figure 3 began to indicate stress concentration in the principal directions at 60% and 70% porosities. Zhang et al.[27] showed that lidinoid structures

undergo large deformation at the surface in contact with the applied load. The large deformation combined with thin-walled structure in lidinoids lead to failure. Therefore, compression strength of lidinoid structures remained between 3 and 11 MPa.

Lidinoid and gyroid structures at 50% and 60% porosity were comparable but a 70% porous gyroid structures showed higher compression strength than its similar lidinoid structure. As previously shown in Figure 3, anisotropy in lidinoid structures is the highest at 70% porosity, making them weak in the direction normal to the applied load. Therefore, any in-plane forces acting on the lattice can cause damage which leads to failure. Further, Downing et al.[41] showed that during uniaxial compression of gyroid structures, helical substructures are responsible for transmitting load along the principal axis accounting for a higher compression strength. In case of the lidinoid structure, stresses are locally concentrated on the thin walls of the structure as shown in Figure 4c, leading to damage and hence failure. Further the mid-surface offset required for achieving porosities between 50% and 70% are twice that of split-P and gyroid structures, which reduces the effective thickness and material density distribution, leading to lower compression strength.

Split-P structures at 50% porosity showed the highest compression strength (22.7 ± 4.9 MPa), while structures at 60 and 70% showed similar values of 11.0 ± 1.2 MPa and 11.5 ± 3 MPa respectively. Distribution of maximum principal stresses (shown in Figure 4b) appears to be a combination of helical pattern observed in gyroid structures and also locally distributed within the structure, making them capable of handling higher compressive forces. Pore sizes in these structures were between 0.1 and 0.15 mm in both structures and further their predicted stiffness matrix showed a similar response for both these structures (shown in Figure 3). Rezapourian et al.[42] showed that failure in split-P structures begin at the highest layers (top/bottom) and experience stretching and shearing during compression load, but extent of the stretching is a function of the relative density of the lattice. Therefore, increasing porosity, reduces the strength of these structures, allowing for easier stretching and bending of the lattice. However, in case of brittle materials such as HAp, small amounts of bending or stretching introduces defects within the lattice leading to early failure.

Orientation of the lattice struts in split-P and gyroid structures in the direction of an applied compressive load enables it to have higher compression strength as previously mentioned. Whereas to function as an effective BTE scaffold, compression strength of the scaffold must be coupled with its ability to interact with its surroundings. Interaction with the local niche enables a bone healing cascade, triggering cells to repair damaged tissue and integrate the implanted scaffold. The simulated body fluid test described in the next sections provides an indication of potential osteoconductivty of the scaffold material. This test as described in previous studies[43] only measures the ability of the scaffold to promote the deposition of bone-like apatite on its surface, which is indicative of its potential to support bone regeneration in vivo.

3.3. Simulated Body Fluid Test

The simulated body fluid (SBF) solution used during this study, is known to simulate the ionic conditions of human blood plasma. Previous studies have shown that in vivo apatite formation observed in sintered hydroxyapatite can be closely replicated using SBF.[43,44] The supersaturated solution consisting of calcium and phosphates undergoes precipitation as a function of changes in physiological conditions such as nucleation time, solution pH, and interfacial energy.[20] In **Figure 5** shows the effect of scaffold geometry and porosity on the concentration of calcium (Ca) and Phosphorous (P) ions in the solution. The calcium in the SBF solution is present in the form $CaCl_2$ and the phosphorus is mainly present in the form of phosphates from K_2PO_4. Therefore, the concentration of P and Ca of the solution were closely measured using ICP-MS, finally after 5 weeks of immersion surface of the structures were analyzed using SEM-EDS.

One of the indicators that determines the quantity of HAp precipitated on the scaffold surface is the calcium and phosphate ions present in the solution containing the immersed TPMS structures. Kim et al.[23] showed that after initial soaking of HAp surfaces, the scaffold surface interacted with the surrounding Ca^{2+} ions in the SBF solution. Negative surface charges of the HAp scaffolds attract the Ca^{2+} ions forming the Ca-rich amorphous calcium phosphate (ACP). The formation of the ACP enables the scaffold to interact with the negatively charged phosphate ions (PO_4^{2-}) in SBF. Low stability of the amorphous phase in aqueous solution causes the transformation to an apatite crystal phase. After the formation of the apatite, the calcium, phosphate, magnesium, and sodium ions present in the SBF lead to the growth of apatite crystal.[21,23]

The ICP-MS results showed that there is decline in Ca^{2+} ion concentration in the 1st week of immersion across all TPMS structures and porosities (as shown in Figure 5b). The Ca^{2+} concentration in the 1st week decreased with increasing porosity across all TPMS structures. Previous studies using hydroxyapatite – 316 stainless steel composites showed an increase in Ca^{2+} concentration due to dissolution of the surface hydroxyapatite layer.[21,23] When immersion time was increased to 2 weeks, there was a gradual increase in Ca^{2+} ion concentration compared to the reference value taken prior to the start of the test. A similar increase in PO_4^{2-} ion content is observed between weeks 1 and 2 across all TPMS structures (shown in Figure 5a). This increase can be attributed toward the dissolution of calcium phosphates into the SBF solution in form of Ca^{2+} and PO_4^{-} ions. As mentioned previously, rate of dissolution of HAp is higher than the rate of precipitation at the initial stages leading to an increase in ion concentration in the measured solution. Increase in Ca^{2+} concentration observed in gyroid and lidinoid structures were proportional to the porosity of the structure. However, the split-P structure showed almost no change with increasing porosity. Lidinoid structures shown in **Figure 6a** have the highest surface area followed by split-P and gyroid structures, but this does not have a direct impact on the dissolution of Ca^{2+} and PO_4^{2-} ions into the SBF solution in week 2.

In weeks 3 and 4, the concentration of Ca^{2+} is shown to plateau across all structures but are still higher than the reference concentration of 90.9 ppm (as shown in Figure S1, Supporting Information). The dissolution of surface HAp layer and the precipitation of HAp is a dynamic process that continues to occur until equilibrium is reached. Initially, as shown, the dissolution of the surface HAp layer outpaces the precipitation of HAp on the scaffold surface. When the reaction approaches equilibrium, the

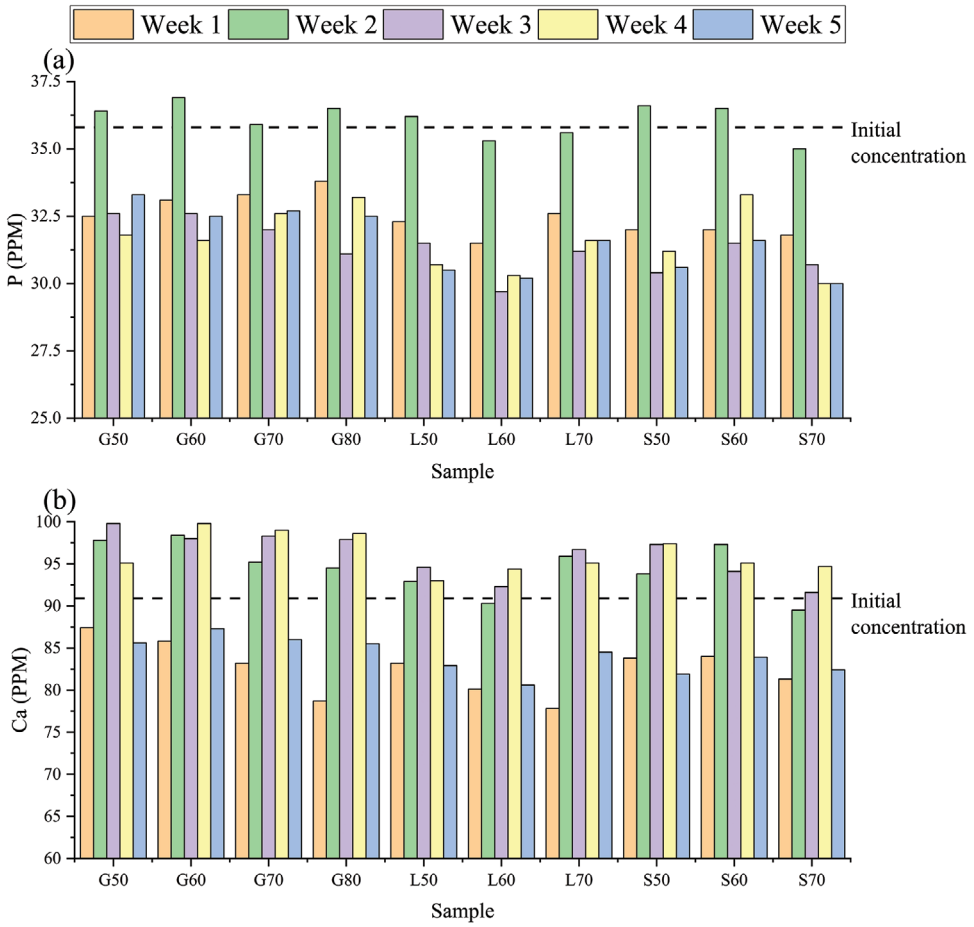

Figure 5. Measured concentration of a) P & b) Ca^{2+} ions in the SBF solution over 5 weeks as function of the TPMS structure porosity. The initial concentration of P and Ca^{2+} ions in the SBF solution has been indicated to be at 35.8 and 90.0 ppm, respectively.

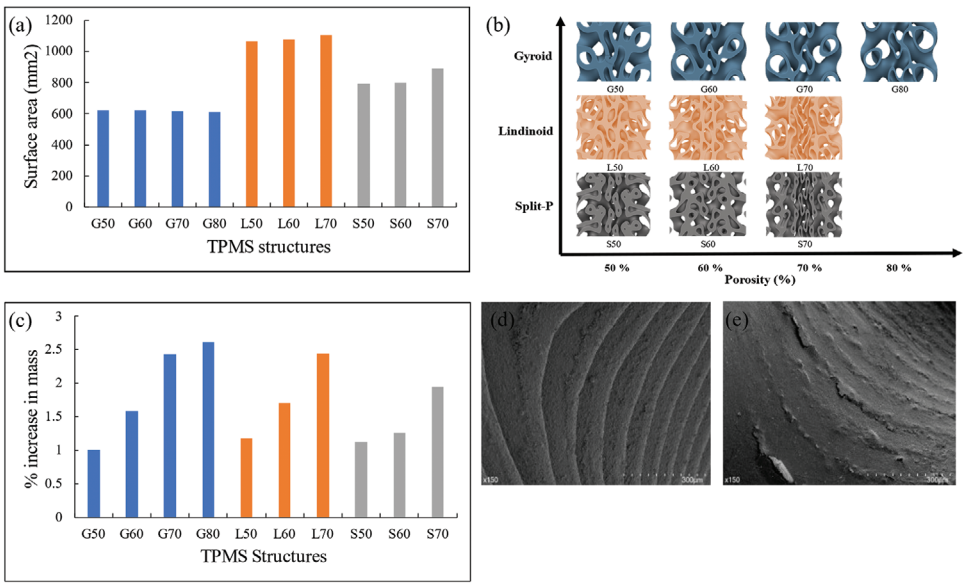

Figure 6. a) Theoretical surface area calculated for the TPMS structures; b) Internal architecture of the TPMS structures; c) Increase in mass of the TPMS scaffolds after 5 weeks of immersion in SBF. Surface morphology of the d) unsoaked TPMS structure e) soaked TPMS structure observed after 5 weeks of immersion in SBF.

dissolution of Ca^{2+} ions decreases and therefore plateaus which is observed across all porosities and geometries between week 2 and week 4. The gyroid and split-P structures showed a small increase (5–10 ppm) and reached their highest values in week 3 before undergoing a gradual decrease from week 4. In week 5, there was a decrease in Ca^{2+} concentration in the SBF solution across all structures and porosities, due to the calcium apatite precipitation on the surface of these scaffolds (this is discussed further in Section 3.3.1). As described previously, with the formation of the apatite crystals from the ACP there is a spontaneous increase in the consumption of Ca^{2+} ions, this is further extended to Mg^{2+} ions that undergo a gradual decrease in concentration in the SBF solution from week 2 onward across all TPMS structures and porosities (shown in Figure S3, Supporting Information).

Phosphorus content of the SBF solution shown in Figure 5a showed an initial reduction in week 1 across all TPMS structures and porosities. Week 2 shows a slight increase (<5 ppm) in P content, this could be attributed to the dissolution of the hydroxyapatite into the SBF solution. A similar increase was observed in Ca^{2+} ions during the same time interval. Xin et al.[21] showed that the dissolution and precipitation of apatite on the surface of the scaffold is a dynamic process, which involves the dissolution of the surface layer increasing the Ca^{2+} ion concentration and the pH of the solution (due to OH^- ions). Spontaneous apatite precipitation begins to occur when the pH is over 7.4, leading to the consumption of Ca^{2+} and PO_4^- ions from the SBF solution to form apatite precipitates.[23] This study shows a similar trend where the P ion content reduction began from week 2 and reached a constant value by week 3. Indicating that significant amount of apatite precipitation occurred during this stage of the process. The next section describes the influence of scaffold geometry on bone apatite precipitation during SBF immersion.

3.3.1. Effect of TPMS Geometry on Apatite Precipitation

Surface area of the TPMS lattice structure is a function of scaffold porosity and pore sizes. Figure 6a describes the variation in the theoretical surface area (SA) of the TPMS structures (extracted from nToplogy software). Variation of the SA within each TPMS structure (gyroid, lidinoid and split-P) are <2%. However, variation across TPMS structures at the same porosities are between 40% and 80%. The internal architecture of the TPMS structures shown in Figure 6b, shows a reduction in closed porosity as the overall porosity increases from 50% to 70%. Gyroid and lidinoid structures of porosities 60% and 70% showed the highest increase (up to 2.5%) in mass after 5 weeks of immersion in the SBF fluid. Whereas split-P structures showed the lowest quantity of apatite precipitation.

Presence of closed porosities at the core of split-P structures shown in Figure 6b reduces its interaction with SBF, hence reducing quantity of apatite precipitation observed. For example, in Figure 6b, the access to interior channels presents in the split-P structure appear to be fewer in comparison to gyroid and lidinoid structures at 60% porosity. Therefore, ease intrusion into the TPMS structure is a critical criterion for the selection of lattice architecture for BTE scaffolds. Split-P structure showed low apatite precipitation even though available surface area was higher than the gyroid structures. Primary reason for this is due to the presence of closed porosities in the split-P structures (as shown in Figure 6b) preventing interaction with the surrounding fluid for precipitation to occur. Similarly, the same effect can be observed in the lidinoid structures where the percentage mass increase (shown in Figure 6c) is identical to that of the gyroid structure while its surface area is significantly higher. This indicates that interconnectivity of the scaffold structure and presence of open porosities are a better indicator of apatite precipitation as opposed to total surface area. Further, only surfaces fully exposed to the SBF fluid underwent changed in surface morphology (as shown in Figure 6e) indicating that interconnectivity that enables higher contact area with the SBF fluid can provide a better surface for precipitation to occur.

Figure 7a shows that precipitates along the surface of the HAp appear in form of spherulites, aggregated masses, and fibers. Ofkeli et al.[45] showed that porous chitosan/gelatin composite cryogels when immersed in a SBF solution for 7 days, produced a mineralized hydroxyapatite coating in the form of spherules. These spherules are petal-like structures that are known to aggregate over the surface. These spherules are observed in Figure 7 however they appear to be distributed and not as individual masses as shown by Ofkeli et al.[45] Hydroxyapatite/collagen coated titanium scaffolds showed a uniform deposition of HAp on the surface of the immersed structure. The rough surface of the coated titanium scaffolds tended to have higher quantity of apatite precipitation.[46] A similar outcome was observed in our study where the apatite precipitation was preferentially deposited on the curved and rough edges as opposed to the flat surfaces on the TPMS structure (as shown in **Figure 8**). Vargas-Becerril et al.[47] showed that initial precipitation of apatite in the form of plate or sheet-like morphology. These initial plates or sheet-like structures functioned as nucleation sites producing thicker layers of apatite precipitation with increasing immersion time. Similarly, the TPMS structures show formation of small plate-like structures as shown in Figure 7b, which eventually form homogenous distribution of apatite precipitate or fibres. Precipitation was primarily observed along the curved surfaces of the TPMS scaffold while flat surfaces of the scaffold show little to no precipitation as shown in Figure 8. Surface texture of the curved surfaces provide higher surface area to interact with the surrounding medium, thus allowing for higher precipitation. Furthermore, rough surfaces are known to promote the precipitation of HAp during SBF immersion which is indicated in Figure 8.[48]

Different types of precipitates on the surface of TPMS structures after 5 weeks of immersion in SBF are shown in Figure S6 (Supporting Information). Formation of these precipitates are driven by the reactions described previously (in Section 3.3); EDS was used to confirm the chemical nature of these precipitates. Ca/P ratio at the surface of the unsoaked sample (as shown in **Figure 9**a) was 1.49 ± 0.02 which is the typical value reported for HAp with trace amounts of cationic impurities such as Mg.[49] Marques et al.[49] showed that localized pH of the solution has a major impact on the mineralization of HAp. EDS spectrum collected at different precipitates showed that Ca/P ratio of the precipitates were different depending on the local conditions. For example, EDS spectrum measured and shown in Figure 9c,d showed an average Ca/P ratio of 1.4 ± 0.02 (measured at 6 dif-

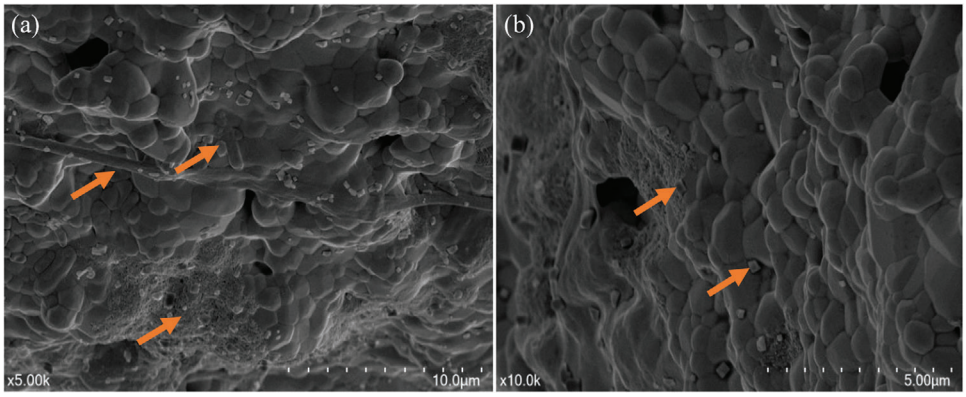

Figure 7. a) Apatite precipitation observed in the form of spherules, fibers, and aggregated masses after 5 weeks of immersion. b) Nucleation sites for further apatite precipitation.

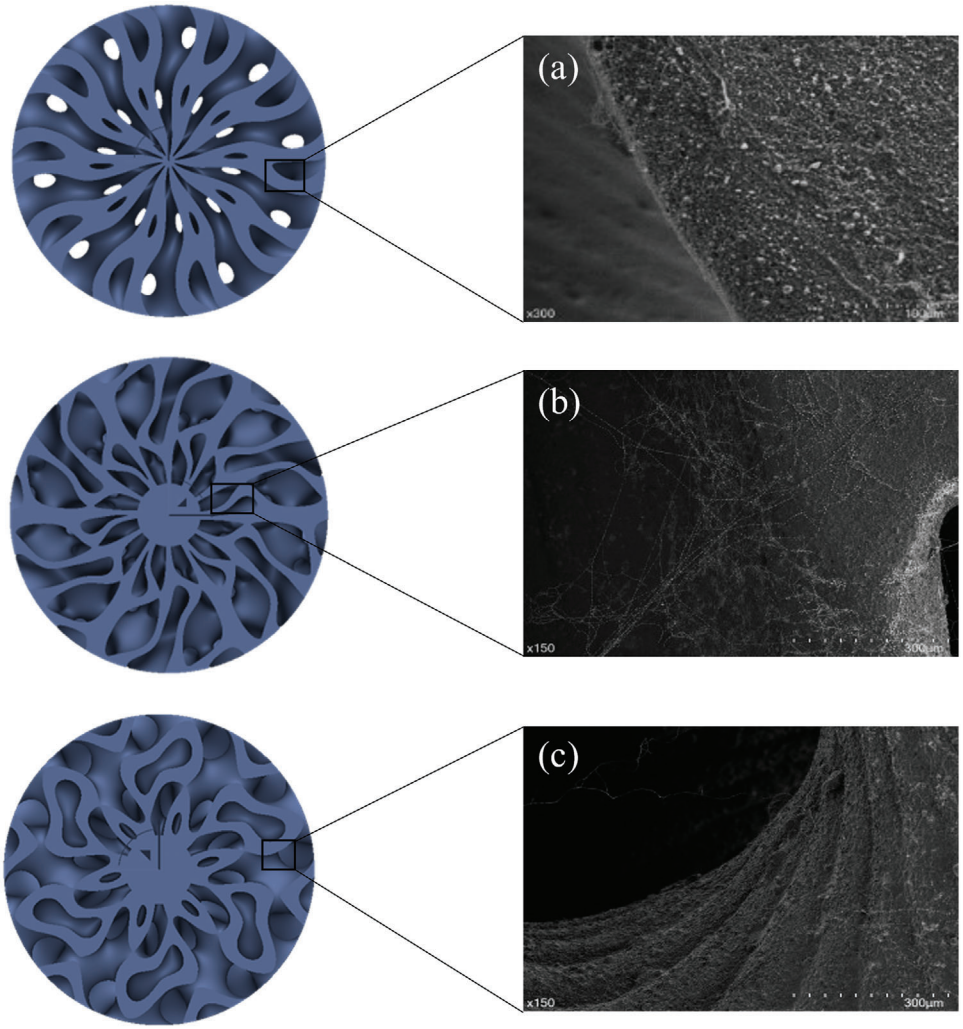

Figure 8. Precipitation of bone apatite on the surface of a) gyroid b) lidinoid and c) split-P architectures. Apatite precipitation observed in all structures show a tendency toward undergoing precipitation along the curved faces of the TPMS structures.

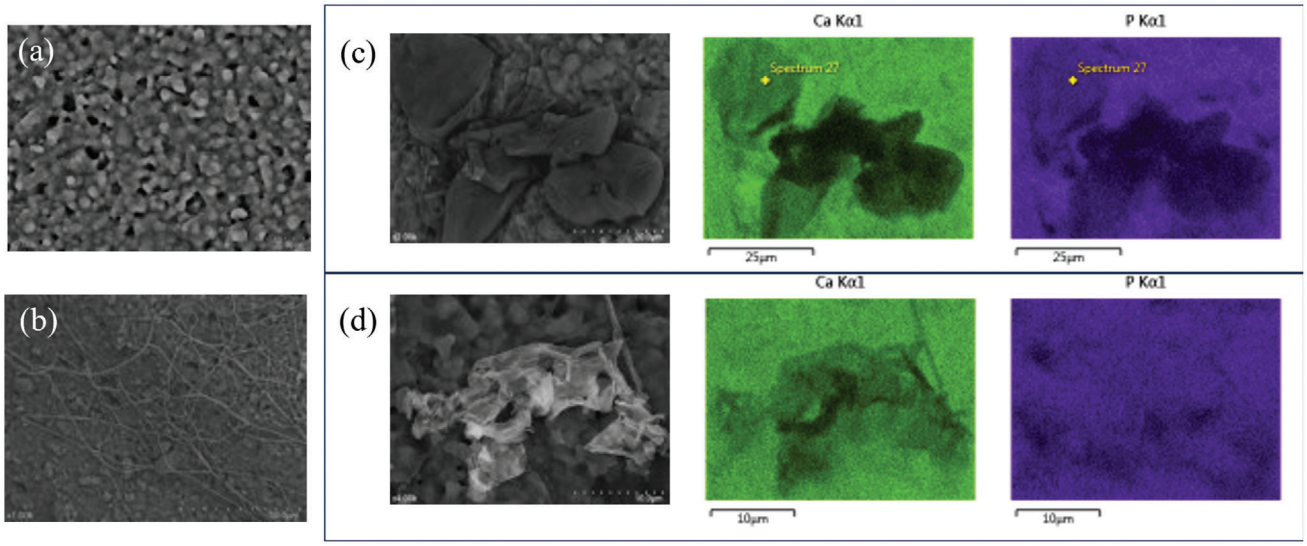

Figure 9. a) SEM image of the unsoaked sample. b) SEM image of soaked samples with string-like precipitates. EDS mapping of the solid precipitates observed across the surface of the sample (c) and (d).

ferent spots), which is similar to the Ca/P ratio reports for octacalciumphosphate ($Ca_8(H_2(PO_4)_6.5H_2O$). Further, formation of a calcium deficient phosphates can be observed is different areas of the surfaces, EDS mapping of the precipitates showed a reduction in the intensity of Ca, indicating the precipitation of octacalciumphosphates. Whereas string-like precipitates observed in Figure 9b showed a higher Ca/P ratio of 1.63 ± 0.06, which is higher than the reported value for the unsoaked HAp sample. Marques et.al[49] showed that a higher Ca/P ratio of 1.6 was observed during the formation of calcium-deficient carbonate apatite. Substitution of PO_4^{2-} ions by CO_3^{2-} ions reduces the amount atomic phosphorus leading to a higher Ca/P ratio. Therefore, nature of the chemical nature of the precipitate is function of the localized pH of the SBF fluid. There was no conclusive link between the scaffold architecture and the chemistry of the precipitate as the local conditions of each precipitation site would be unique.

3.4. Graded TPMS Structures

Graded TPMS structures provide significant advantage compared to single architectures due to their multi-functionality. Load bearing BTE applications require a compression strength of at least 100 MPa while also providing sufficient porosity for the infiltration of the extracellular matrix and bone in-growth.[2,50] Split-P structures at 50% porosity appeared to have the highest mechanical strengths (22.7 ± 4.9) while G70, L70, and G80 structures showed the highest apatite precipitation on the scaffold surface. Therefore, the core of the scaffold was designed using the structure with the highest compression strength while the outer shell was designed with TPMS structures that provided the highest apatite precipitation ability. Their compression strength and cellular proliferation were compared with structures having a solid core of diameter 3.5 mm while having an outer shell with G70, G80 and L70 architectures.

3.4.1. Compression Strength

The graded composite structures with porous cores (S50) show a compression strength <10 MPa, which is significantly lower than the previously analyzed TPMS structures (Section 3.2). Whereas structures with solid cores show compression strengths in the range of 50–120 MPa, which is close to the mechanical strength required for load bearing application in BTE.[27] In this study the G70 structure with a solid core showed the highest compression strength of 122 MPa. Further the pore sizes of the outer shell were in the range of 0.9–1.2 mm and had a porosity of 70% allowing for cell penetration and bone in-growth during implantation.[50] Zhang et al.[27] showed a mechanical strength of 150 MPa using the split-P structure but at an average pore size of 0.3 mm and a porosity of 50%. Arabnejad et al.[50] achieved a compression strength of up to 120 MPa at a pore size of 0.5 mm and porosity of 70% using tetrahedrons made from Ti6Al4 V alloy. Furthermore, pore sizes of 0.77 mm in the octet trusses reduced its compression strength to 31 MPa. In this study, the G80 structures with pore sizes between 0.9 and 1.8 mm produced a compression strength of 73.8 ± 3.8 MPa. TPMS structures with solid cores are more suitable for load bearing BTE applications.

Porous cored structures shown in **Figure 10**a,b, were created by blending a core with the split-P architecture with an outer shell having lidinoid and gyroid architectures, respectively. Weak contact observed between the two structures as seen in Figure 10a,b indicates the relative ease in crack formation compared to the structures with the solid core. The structures with solid cores, show higher compression strength and offers higher contact area with the outer shell. Thus, G70 structures with a solid core having a compression strength of 122 MPa appears to the ideal configuration for load bearing BTE applications. Compression strengths obtained for solid cored samples are stronger or close to human cortical bone but significantly stronger than solid 3D printed HAp (shown in Figure 10f). In the next section, their effect of the

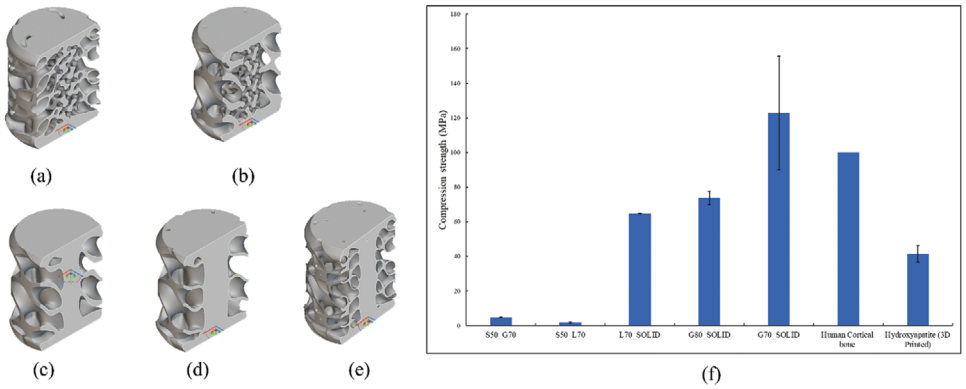

Figure 10. Graded TPMS structure having an inner core of S50 with a diameter of 3.5 mm and an outer shell made from structures a) L70 and b) G70. TPMS structure with a solid core of diameter 3.5 mm and an outer shell made from structures c) G70, d) G80, and e) L70. f) Measured compression strength of the solid cored TPMS and graded TPMS structures.

solid and porous core in proliferation of osteoblast cells will be examined.

3.5. In Vitro Testing

3.5.1. Proliferation Assay

Proliferation of human osteoblasts on the TPMS structures was determined by measuring the reduction of resazurin to resofurin. The absorbance was measured against wells only with cells at intervals of 1, 3, and 10 days (shown in **Figure 11a**). All scaffolds on day 1 showed similar cell viability compared to the well plate. Day 3 showed the highest increase in cell activity across all structures and reference wells. The osteoblast cells appeared to have infiltrated the inner core of the structures as shown in Figure 11c, whereas structures with solid cores only showed attachment at the edge of the solid core and other areas as shown in Figure 11d. This could be due to ease of nutrient availability at the outer diameters of the porous sample,[51] while the core structures do not receive sufficient nutrients resulting in a minor drop in for supporting cell proliferation after day 3. A student t- test was used to compare the observed reduction values in porous and solid core samples, the obtained p-value (0.3853) was significantly larger than 0.05, indicating that cells show a similar viability irrespective of the cores being porous or solid. Similarly, when the percentage reduction in solid core samples were compared with cell only reference values using a student t-test. The obtained p-value (0.4815) was significantly larger than 0.05, indicating that there is no statistical difference in the viability of osteoblast cells. While the scaffolds tested did not produce any statistically significant variation at the measured intervals, recent studies have shown that micro and/or nanoscale features influence cell attachment and fate.[52,53] Cell attachment being a multistep process, quality of each step influences the next resulting in continuous proliferation or loss.[54] Therefore, future studies

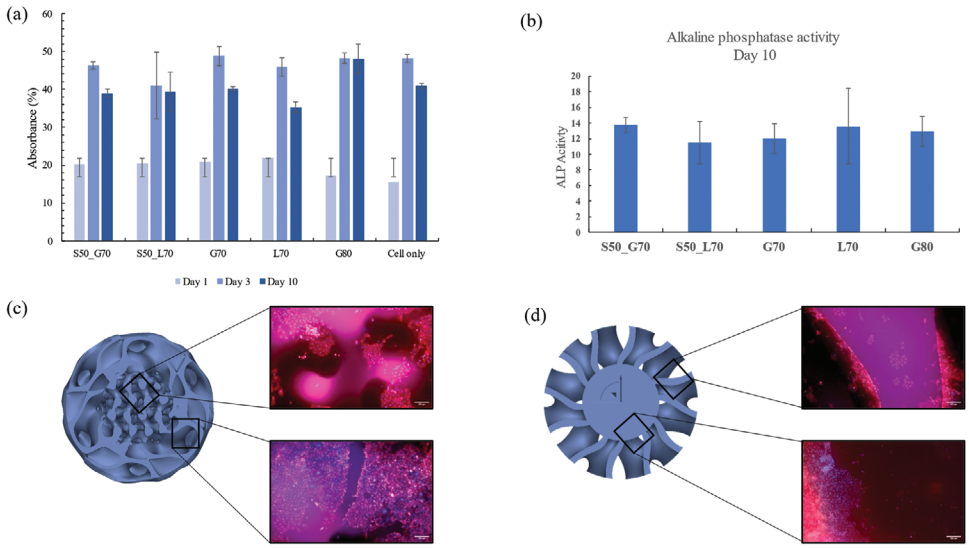

Figure 11. a) Cell proliferation of the composite TPMS structures compared to a cell only reference. b) ALP activity of osteoblast cells measured on day 10 cultured on the solid cored and porous cored scaffolds. Osteoblast cells attachment at the outer shell and the inner sections of the scaffold for c) S50-L70 structure and d) Solid core with G70 structure.

must take into account the nanoscale features intentionally or unintentionally introduced during the manufacturing process while analyzing cell proliferation in BTE scaffolds.

ALP activity of the cells measured at day 10 during culture in an osteogenic medium is shown in Figure 11b. Structures show similar levels of ALP activity with minor variations within the range of their standard deviation. Observation of ALP activity in the cultured osteoblast cells mark the different stages of osteoblast maturation and help mediate deposition of hydroxyapatite.[55,56] While there are other multiple regulatory factors that are responsible for bone forming, expression of ALP has been a common factor primarily because glycoproteins such as ALP help separate inorganic phosphates that then combine with the available Ca^{2+} ions to form hydroxyapatite, thereby integrating the scaffold structures to the damaged bone tissue.[57,58] Although ALP activity cannot confirm bone in-growth, its presence alongside the scaffold structures indicates that there is no barrier to the cells forming bone tissues. Graded and solid core samples placed in a differentiation medium after 10 days showed similar ALP activity irrespective of their core design. Therefore, signals OF the osteogenic potential of these TPMS lattice structures are not affected by the core design.

Structures G70 and G80 with the solid core provide similar performance when compared to the structures with a porous core. Further the G70 solid core structure provides a compression strength over 100 MPa making it an ideal choice for load bearing BTE applications.

4. Conclusion

This study shows the performance of TPMS structures (gyroid, lidinoid, split-P) during apatite precipitation and determined their mechanical properties at porosities (50%, 60%, and 70%) and pore sizes (0.9–1.8 mm). Large pore sizes and high interconnectivity of G70, G80, and L70 structures, showed the highest increase in mass after 5 weeks of immersion in the SBF fluid. Further their ability to interact or undergo apatite precipitation was due to a combination of high porosity and interconnectivity, enabling ions transfer between the fluid and the scaffold surface. While this study showed the extent of apatite precipitation observed in different

Mechanical performance of these TPMS structures were lower than 30 MPa across all porosities and pore sizes, making them unsuitable to be used for load bearing BTE applications, rather only offering mechanical performance similar to trabecular bone. Solid-cored TPMS structures, designed to leverage their apatite precipitation capability and enhance compressive strength, demonstrated mechanical performance (122 MPa) suitable for load-bearing applications in bone tissue engineering (BTE) at high porosities (70%) and large pore sizes (0.9–1.5 mm). Furthermore, cellular assays showed that cytoxicity and ALP activity of solid core samples (G70, L70, and G80) remained identical to their porous cored alternatives. However, influences of nanoscale features introduced during 3D printing and sintering on cell proliferations need to be understood in future studies. In vivo studies on rodent models can provide an insight the scaffold ability to assist the bone healing response. Large animal models can help shed light on the biomechanical response during loading and long-term effects on hydroxyapatite resorption.

Cellular penetration in porous cores structures remained marginally better as shown from the microscopic images captured, their poor compression strength makes them unsuitable for use in load bearing BTE applications. The poor compression strength of porous cored structures is (<20 MPa) due to insufficient contact area between the core and shell. Since the porous cored structures can provide further bone in-growth and mechanical interlocking to provide long term structural support for the damaged bone tissue. Further work is required to identify suitable blending strategies between the TPMS structures to improve mechanical performance. These blending strategies could be applied to the solid core samples, reducing the diameter of solid core and increase the number of pores available for bone in-growth. Lastly, scaffolds used in load bearing application are often subject to multi-directional loading, therefore ability to prevent fracture of the TPMS structures under loading could be a better indicator of the mechanical performance as opposed to only compression strength. These improvements will significantly contribute toward building a truly multi-functional scaffold for load bearing application in BTE.

Supporting Information

Supporting Information is available from the Wiley Online Library or from the author.

Acknowledgements

The authors very thankful to Daniel J. Browne for his invaluable assistance in carrying out fluorescence microscopy. His collaboration and assistance were vital to the completion of this study. This research did not receive any specific grant from funding agencies in the public, commercial, or not-for-profit sectors.

Open access publishing facilitated by James Cook University, as part of the Wiley - James Cook University agreement via the Council of Australian University Librarians.

Conflict of Interest

The authors declare no conflict of interest.

Data Availability Statement

The data that support the findings of this study are available from the corresponding author upon reasonable request.

Keywords

3D Printing, bioceramic, bone tissue engineering, graded structures

Received: August 8, 2024
Revised: January 30, 2025
Published online: February 14, 2025

[1] J. J. Li, M. Ebied, J. Xu, H. Zreiqat, *Adv. Healthcare Mater.* **2018**, *7*, 1701061.

[2] T. M. Koushik, C. M. Miller, E. Antunes, *Adv. Healthcare Mater.* **2022**, *12*, 2202766.
[3] M. Mohammadi Zerankeshi, S. Mofakhami, E. Salahinejad, *Ceram. Int.* **2022**, *48*, 22647.
[4] J. Zhang, D. Tong, H. Song, R. Ruan, Y. Sun, Y. Lin, J. Wang, L. Hou, J. Dai, J. Ding, H. Yang, *Adv. Mater.* **2022**, *34*, 2202044.
[5] G. Jia, H. Huang, J. Niu, C. Chen, J. Weng, F. Yu, D. Wang, B. Kang, T. Wang, G. Yuan, H. Zeng, *J. Magnesium Alloys* **2021**, *9*, 1954.
[6] F. Fendi, B. Abdullah, S. Suryani, A. N. Usman, D. Tahir, *Bone* **2024**, *183*, 117075.
[7] D. Jeyachandran, M. Cerruti, *Adv. Eng. Mater.* **2023**, *25*, 2201743.
[8] M. Draenert, A. Draenert, K. Draenert, *Microsc. Res. Tech.* **2013**, *76*, 370.
[9] C. R. Kruse, M. Singh, S. Targosinski, I. Sinha, J. A. Sørensen, E. Eriksson, K. Nuutila, *Wound Repair Regener.* **2017**, *25*, 260.
[10] W. Busa, R. Nuccitelli, *Am. J. Physiol.: Regul., Integr. Comp. Physiol.* **1984**, *246*, R409.
[11] S. Grinstein, D. Rotin, M. J. Mason, *Biochimica et Biophys. Acta (BBA) – Rev. Biomembr.* **1989**, *988*, 73.
[12] I. A. Silver, J. Deas, M. Erecińska, *Biomaterials* **2001**, *22*, 175.
[13] G. Spence, N. Patel, R. Brooks, N. Rushton, *J. Biomed. Mater. Res., Part A* **2009**, *90A*, 217.
[14] C. Knabe, M. Stiller, M. Kampschulte, J. Wilbig, B. Peleska, J. Günster, R. Gildenhaar, G. Berger, A. Rack, U. Linow, M. Heiland, C. Rendenbach, S. Koerdt, C. Steffen, A. Houshmand, L. Xiang-Tischhauser, D. Adel-Khattab, *Front. Bioeng. Biotechnol.* **2023**, *11*, 1221314.
[15] D. Pierantozzi, A. Scalzone, S. Jindal, L. Stipniece, K. Salma-Ancane, K. Dalgarno, P. Gentile, E. Mancuso, *Compos. Sci. Technol.* **2020**, *191*, 108069.
[16] E. Mancuso, L. Shah, S. Jindal, C. Serenelli, Z. M. Tsikriteas, H. Khanbareh, A. Tirella, *Mater. Sci. Eng., C* **2021**, *126*, 112192.
[17] A. A. Zadpoor, *Mater. Sci. Eng., C* **2014**, *35*, 134.
[18] E. Ellermann, N. Meyer, R. E. Cameron, S. M. Best, *Regenerat. Biomater.* **2023**, *10*, rbad027.
[19] H. Pan, X. Zhao, B. W. Darvell, W. W. Lu, *Acta Biomater.* **2010**, *6*, 4181.
[20] X. Lu, Y. Leng, *Biomaterials* **2005**, *26*, 1097.
[21] X. Fan, J. Chen, J.-P. Zou, Q. Wan, Z.-C. Zhou, J.-M. Ruan, *Trans. Nonf. Metals Soc. China* **2009**, *19*, 347.
[22] T. Kokubo, H. Takadama, *Biomaterials* **2006**, *27*, 2907.
[23] H.-M. Kim, T. Himeno, T. Kokubo, T. Nakamura, *Biomaterials* **2005**, *26*, 4366.
[24] T. M. Koushik, C. M. Miller, E. Antunes, *Adv. Healthcare Mater.* **2023**, *12*, 2202766.
[25] M. Fantini, M. Curto, F. De Crescenzio, *Virtual Phys. Prototyping* **2016**, *11*, 77.
[26] L. Germain, C. A. Fuentes, A. W. van Vuure, A. des Rieux, C. Dupont-Gillain, *Mater. Des.* **2018**, *151*, 113.
[27] Q. Zhang, L. Ma, X. Ji, Y. He, Y. Cui, X. Liu, C. Xuan, Z. Wang, W. Yang, M. Chai, X. Shi, *Adv. Funct. Mater.* **2022**, *32*, 2204182.
[28] Y. Feng, T. Huang, Y. Gong, P. Jia, *Mater. Des.* **2022**, *222*, 111078.
[29] J. Walles, *What equations are used to create the TPMS types? ,nTopSupport 2024*, https://support.ntop.com/hc/en-us/articles/360053267814-What-equations-are-used-to-create-the-TPMS-types.
[30] T. Koushik, E. Antunes, in *Advanced Flexible Ceramics*, (Ed: R. K. Gupta), Elsevier, Amsterdam, The Netherlands **2023**, pp. 193–214.
[31] A. Oyane, H.-M. Kim, T. Furuya, T. Kokubo, T. Miyazaki, T. Nakamura, *J. Biomed. Mater. Res., Part A* **2003**, *65A*, 188.
[32] J. O'Brien, I. Wilson, T. Orton, F. Pognan, *Eur. J. Biochem.* **2000**, *267*, 5421.
[33] S. N. Rampersad, *Sensors* **2012**, *12*, 12347.
[34] F. Ren, E. D. Case, A. Morrison, M. Tafesse, M. J. Baumann, *Philos. Mag.* **2009**, *89*, 1163.
[35] L.-H. He, O. C. Standard, T. T. Y. Huang, B. A. Latella, M. V. Swain, *Acta Biomater.* **2008**, *4*, 577.
[36] S. Khaleghi, F. N. Dehnavi, M. Baghani, M. Safdari, K. Wang, M. Baniassadi, *Mater. Des.* **2021**, *210*, 110074.
[37] G. Holzer, G. von Skrbensky, L. A. Holzer, W. Pichl, *J. Bone Miner. Res.* **2009**, *24*, 468.
[38] S. M. Ott, *Am. J. Nephrol.* **2018**, *47*, 373.
[39] S. S. Scherrer, U. Lohbauer, A. Della Bona, A. Vichi, M. J. Tholey, J. R. Kelly, R. van Noort, P. F. Cesar, *Dental Mater.* **2017**, *33*, 599.
[40] D. W. Abueidda, M. Elhebeary, C.-S. Shiang, S. Pang, R. K. abu Al-Rub, I. M. Jasiuk, *Mater. Des.* **2019**, *165*, 107597.
[41] D. Downing, A. Jones, M. Brandt, M. Leary, *Mater. Des.* **2021**, *197*, 109096.
[42] M. Rezapourian, I. Jasiuk, M. Saarna, I. Hussainova, *Int. J. Mech. Sci.* **2023**, *251*, 108353.
[43] F. Baino, S. Yamaguchi, *Biomimetics* **2020**, *5*, 57.
[44] T. Kokubo, *Biomaterials* **1991**, *12*, 155.
[45] F. Öfkeli, D. Demir, N. Bölgen, *J. Appl. Polym. Sci.* **2021**, *138*, 50337.
[46] D. J. Patty, A. D. Nugraheni, I. Dewi Ana, Y. Yusuf, *Bone Tissue Eng. Bioeng.* **2022**, *9*, 784.
[47] N. Vargas-Becerril, D. A. Sánchez-Téllez, L. Zarazúa-Villalobos, D. M. González-García, M. A. Álvarez-Pérez, C. de León-Escobedo, L. Téllez-Jurado, *Ceram. Int.* **2020**, *46*, 28806.
[48] L. Liu, F. Ma, B. Kang, P. Liu, S. Qi, W. Li, K. Zhang, X. Chen, *Surf. Coat. Technol.* **2023**, *463*, 129530.
[49] P. Marques, M. Magalhães, S. V. Dorozhkin, R. N. Correia, *Key Eng. Mater.* **2001**, *27*, 192.
[50] S. Arabnejad, R. Burnett Johnston, J. A. Pura, B. Singh, M. Tanzer, D. Pasini, *Acta Biomater.* **2016**, *30*, 345.
[51] N. Sarkar, S. Bose, *Acta Biomater.* **2020**, *114*, 407.
[52] K. Anselme, M. Bigerelle, *Acta Biomater.* **2005**, *1*, 211.
[53] B. Altmann, R.-J. Kohal, T. Steinberg, P. Tomakidi, M. Bächle-Haas, A. Wennerberg, W. Att, *Tissue Eng., Part C* **2013**, *19*, 850.
[54] K. Rabel, R.-J. Kohal, T. Steinberg, P. Tomakidi, B. Rolauffs, E. Adolfsson, P. Palmero, T. Fürderer, B. Altmann, *Sci. Rep.* **2020**, *10*, 12810.
[55] A. Piattelli, A. Scarano, M. Corigliano, M. Piattelli, *Biomaterials* **1996**, *17*, 1443.
[56] J. Jaroszewicz, J. Idaszek, E. Choinska, K. Szlazak, A. Hyc, A. Osiecka-Iwan, W. Swieszkowski, S. Moskalewski, *Mater. Sci. Eng., C* **2019**, *96*, 319.
[57] S. Boonrungsiman, E. Gentleman, R. Carzaniga, N. D. Evans, D. W. McComb, A. E. Porter, M. M. Stevens, *Proc. Natl. Acad. Sci. USA* **2012**, *109*, 14170.
[58] S. Ansari, K. Ito, S. Hofmann, *ACS Omega* **2022**, *7*, 12724.